Response of short monopiles for offshore wind turbine foundations: virgin and post-cyclic capacity

Francisco J Grajales, Ryan D Beemer, Madhuri Murali, Charles Aubeny
Zachry Dept. of Civil Engineering, Texas A&M University, USA
Giovanna Biscontin
Department of Engineering, University of Cambridge, UK

GEOQuébec 2015
Challenges from North to South
Des défis du Nord au Sud

ABSTRACT
Geotechnical centrifuge tests were conducted to examine monotonic behavior of low aspect ratio piles in soft clays. Monopiles with aspect ratio of two were tested in the 150g-ton centrifuge at Rensselaer Polytechnic Institute. Initial pile test results include force-displacement for displacement controlled loading. This paper focuses on ultimate capacity of short aspect ratio monopiles after cyclic loading. Post-cyclic monotonic capacity is compared to virgin monotonic capacity for pure rotational loading over a range of eccentricities.

RÉSUMÉ
Des essais géotechniques avec centrifugeuse ont été menés afin d'examiner le comportement des monopieux de faible rapport longueur-diamètre dans les argiles molles. Des monopieux avec un rapport longueur-diamètre de deux ont été testés dans la centrifugeuse de 150g-tonnes au Rensselaer Polytechnic Institute. Les résultats des essais de pieux comprennent les courbes force-déplacement pour le chargement en déplacement contrôlé. Cet article se concentre sur la capacité ultime des monopieux à faible rapport longueur-diamètre après un chargement cyclique. La capacité monotone post-cyclique est comparée à la capacité monotone vierge pour le chargement en rotation pure, et ce sur une plage d'excentricités.

1 INTRODUCTION

Offshore wind power has gained momentum as a means to diversify the world's energy infrastructure; however, little is still known about the global stiffness behavior of the large diameter low aspect ratio monopiles which are becoming a foundation of choice for offshore wind towers. Traditionally, offshore foundations have been associated with oil and gas structures, which in general are not subject to moment loads, unlike wind turbines.

Geotechnical centrifuge tests have been conducted in order to assess the response of short monopile foundations for offshore wind turbines. Both monotonic and cyclic loading conditions have been considered.

This paper covers a specific case of post-cyclic capacity: capacity after one-way low magnitude (working loads) cycling in the opposite direction. The initial goal of this set of tests was to simply investigate the behavior of one-way cyclic loading on squat monopiles. However, after cycling was completed it was decided to run capacity test in the opposite direction of cyclic loading; this was done to protect the pore pressure sensors. The initial hypothesis was that one-way cycling would have little impact of capacity since failure would occur in undisturbed soil; this was not the case.

Cycling in a predominant direction will affect capacity in the opposing direction. These results may be useful for predicting capacity of aged monopiles related to storm loading or vessel collisions. It appears a reduction factor on capacity would be required even if failure were to occur in the opposite direction of predominate wind and wave loading.

2 BACKGROUND

Offshore structures have been traditionally related to the exploration and production of oil and gas (Randall, 2010). These structures range from the very common fixed structures to several more recent systems such as tension leg platforms (TLPs) and SPAR platforms. In addition to oil and gas applications, in recent years interest has been focused on wind energy as an alternative to fossil fuels. Offshore wind farms offer the benefit of more sustained and stronger winds at lower heights, and also they avoid the aesthetic issues common for onshore developments of such a type.

On oil and gas structures, moment loading is not a controlling factor in the design process. Wind turbines however, possess large moment loads (Fig. 1). For this reason, the existent design criteria for oil and gas structures is not applicable for wind towers.

The loads applied on the structure are transferred to the soil, thus, the characteristics of those loads and the properties of the soil govern the size and type of foundations required to support an offshore structure (Schneider and Senders, 2010). Also, the type of foundation depends on the conceptual design of the superstructure. For example: in the case of monopile foundations the lateral and moment loads are transmitted directly to the foundation, creating a moment demand relatively high. On the other hand, for multi-leg systems the moment loading is transferred to each foundation system as either tension or compression, combined with a moment component. However, in this case, since pile foundations perform better under axial loading rather than moment, the piles for multi-leg systems are generally smaller than those for monopile foundations.

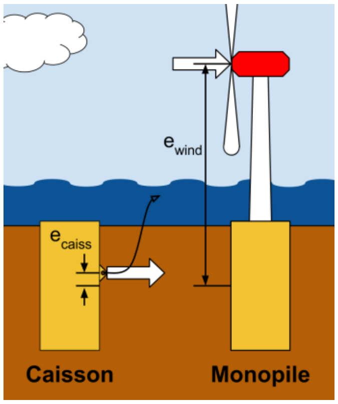

Figure 1. Monopiles loading versus caisson loading

2.1 Foundations for Offshore Structures

Pile foundations are the most commonly used type of foundation for several offshore applications. One reason for this is their reliability for resisting axial and horizontal load. Offshore piles vary widely in both diameter and length, however typical aspect ratios (length to diameter, *L/D*) range from 20 to 70 (Schneider and Senders, 2010) and diameter to wall thickness ratios ranging from 25 to 100.

Most of the oil and gas structures are massive and large, therefore the foundation is designed as an arrangement of piles or in some cases a pile group. On the other hand, monopiles are the prevalent foundation type for offshore wind turbines. Monopile foundations for offshore wind towers require large diameter piles (usually 3 to 6 m) with *L/D* ratios of 4 to 20.

Suction caissons have a cylindrical shape: hollow at the bottom and closed at the top (Andersen, et al., 2005). Aspect ratio normally oscillates between 3 and 8; therefore they are short structures, unlike conventional piles that are rather slender (e.g. *L/D* of 30).

Caissons have been used recently as an alternative to conventional piles due to cost. Several advantages over the latter are: (1) the installation time is shorter and requires less equipment; (2) the manufacturing process normally requires less material because caissons are smaller than piles, therefore, is less expensive; (3) transportation to the site is more efficient than conventional piles since several caissons can fit in the same transportation vessel; and (4) caissons are widely used as anchoring systems for floating structures (such as TLPs and SPARs); however they can also work as foundations for vertically supported offshore structures as is the case of offshore wind turbines.

2.2 Capacity of Laterally Loaded Monopiles

Murff and Hamilton (1993) presented a three dimensional upper bound plastic limit analysis method for the analysis of the ultimate undrained capacity of laterally loaded piles. The analysis accounted for free surface strength reduction and for rotational tip resistance at the bottom of the pile.

The collapse mechanism is composed of three different regions: (1) a surface failure wedge, (2) a flow around zone and (3) a spherical failure surface at the pile tip. Fig. 2 illustrates this three regions. Expressions for internal energy dissipation were then derived based on kinematically admissible velocity fields both in the surface wedge and spherical tip failure. Meanwhile, energy dissipation occurring in the flow around zone was accounted for by using failure criteria proposed by Randolph and Houlsby (1984).

Some of the additional features of the Murff and Hamilton model are: (1) it considers rotation of the pile about a point located at a depth, L_0, (2) the model can accommodate the development of a plastic hinge in the pile, (3) it can model various soil conditions such as soil-pile interface adhesion, suction or no suction at the back of the pile. Finally, four optimization parameters are considered: depth to the center of rotation (L0), depth of the wedge, radial extent of the top of the wedge and radial variation of velocity along the wedge.

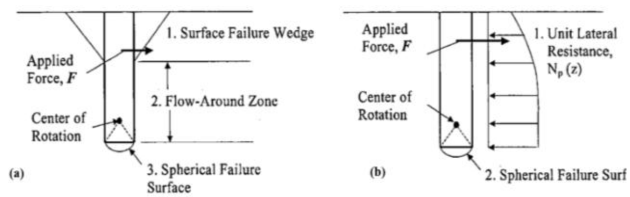

Figure 2: Comparison of failure mechanisms

Murff and Hamilton (1993) upper bound PLA formulation proposes an exponential function in order to characterize the equivalent lateral soil pressure profile along the pile or caisson, as is described in Equation 1. An empirical solution was developed in order to be able to reproduce the values obtained by plastic limit analysis. This solution includes the factor η, which accounts for the variation of soil strength profile. This factor was calibrated by using a non-linear least squares method. Upper bound formulations originally assume that a gap forms behind the caisson. For the case of no gap forming behind the caisson, values obtained with the empirical solution are doubled and limited to N_1, which is a factor computed from Randolph and Houslby (1984).

$$N_{ps} = N_1 - N_2 e^{\left(-\eta z / D\right)} \quad [1]$$

Where: N_1 is the limiting value for pure lateral resistance at a depth sufficient enough that the free surface effects can be neglected. (Randolph and Houlsby, 1984); N_2 is selected such that (N_1 - N_2) is the lateral resistance at the surface; η is a parameter which characterizes the effect of the soil strength profile; z is the depth, and D is the diameter

Based on this empirical solution, Aubeny et al. (2001) developed a simplified upper bound PLA method, intended to be applied for caissons and open ended piles. This method avoids solving the complex integrations required to evaluate the detailed mechanism. Only one optimization parameter is required, the depth to the center of rotation. This reduces in a significantly the computation time required for the analysis. This procedure is limited to the case of either a constant or linearly increasing undrained shear strength profile.

At a given depth increment located at any point along the monopile, the internal rate of energy dissipation is computed by the product of the mobilized pressure times the projected area ($\Delta z\ D$) times the velocity at the point in question. The method is widely discussed in Aubeny et al. (2001), Aubeny et al. (2003) and Aubeny and Murff (2005). A summary of the fundamental mathematical expressions needed to derive energy dissipations for this method is presented in Appendix I.

2.3 Geotechnical Centrifuge Testing

Centrifuge testing has been extensively used to model offshore geotechnical problems (Hamilton, et al., 1991, Murff, 1996, Cluckey, et al., 2004, JeanJean, 2009, Zhang, et al., 2011). It is a well-documented and reliable research tool: Pokrovsky (1936) presented on its use at the 1st International Conference on Soil Mechanics and Foundations. The reason for its success is that it allows prototype magnitude effective stresses to be generated in a scale model, by taking advantage of the linear relationship between gravity and depth. Thus, small scale models can exhibit the same stress dependent behaviors present in the prototype.

3 EXPERIMENTAL SETUP

3.1 Facility

Tests were carried out in the 150 g-ton, 2.7 m nominal radius centrifuge at the Center for Earthquake Engineering Simulations at Rensselaer Polytechnic Institute (Elgamal, et al., 1991). Additionally, the center's four degrees of freedom (DOF) in-flight robot (Ubilla, et al., 2006) was utilized for load application and in-situ testing. For application of load a custom a custom cup adaptor was 3D printed in a Stainless Steel-Bronze alloy (Shapeways, n.d.), Fig. 3. The cup allowed the rotational motion of the monopiles when coupled with the stem.

3.2 Monopiles

The monopiles consist of three components: the caisson, the stem, and the sensors platform, Fig. 4. Caissons were constructed from aluminum tubing turned down to a diameter of 4.96 cm with a wall thickness of 0.61 mm. All monopiles had a plug length of 10.16 cm with an additional 1.27 cm cap welded to the tubing. Resulting in an aspect ratio (*L/D*) of approximately two. Caps were tapped with a vent hole to assist installation and plugged with a small cork while testing. Strain gages were mounted around the circumference of caissons 1.27 cm from the bottom. Strain gage wires were restrained with wrapping and the assembly was coated in rubber.

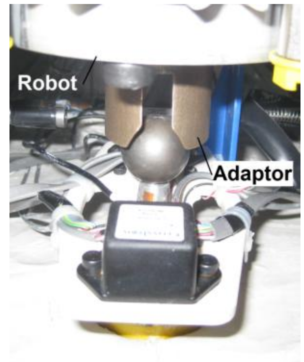

Figure 3. Robot adaptor coupling with rotational stem

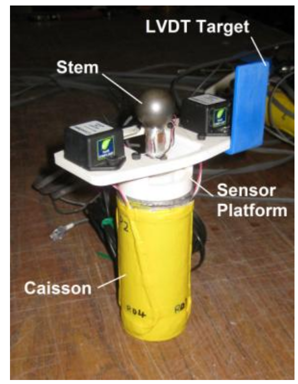

Figure 4. Example pile with components labeled

Stems are rotational in nature with a ball at their end, Fig. 4. They were constructed from either 9.53 mm diameter steel or aluminum rod and were instrumented with strain gauges to measure applied load. Strain gauge wires were restrained with wrapping thread and paint on rubber. Stems where bolted to the aluminum cap allowing them to be interchanged. Stems varied in height from allowing for diameter normalized load eccentricities of approximately 1.25, 2.5, and 3.5 from the pile cap.

The sensor platforms were 3D printed from ABS plastic. They were designed to hold MEMS accelerometers above the model water level and the LVDT target flags. Strain gage wires were also tied to the platforms in order to distribute weight and minimize pulling on the gages themselves. LVDT flags were 3D printed in ABS plastic and fastened to the platform. Two single-axis 10g MEMS accelerometers (MEMSIC, n.d.) were mounted to each platform. These sensors allow measurement of rotation independent of displacement.

3.3 Soil Beds

Both soil beds were constructed in the RPI Large Rigid Boxes, 88cm by 39 cm. Kaolinite clay (BASF ASP 600) was placed at a water content of 80% to a height of 32 cm. The model was then consolidated at 100g to an average water content of 62.2%. Water content distributions for Experiment One with depth, 3 cm from the end of the box, after consolidation is provided in Table 1. Three pore pressure sensors at the mid-depth of the clay were used to monitor pore pressure; approximately 40 kPa was allowed to dissipate. After consolidating the models had an average depth of 25.7 cm. The use of Teflon sheets on the sides of the container resulted in relatively even consolidation, Fig 5. Topography was measured from the top of the box and converted to depth.

After consolidation the models were excavated to a depth of 23 cm. After an expected recompression of 3 cm the expected inflight depth was 20 cm. Soil undrained shear strength was determined, by water content correlation (Tessari, 2012), Stress History and Normalized Soil Engineering Properties (SHANSEP) (Ladd, C. C., and Foott, R., 1974), and inflight T-Bar penetrometer tests (Dejong, et al. 2011). Penetrometer runs were conducted before and after each monopile test Soil strength results for both tests beds are provided in Fig. 6.

3.4 Model Layout

Each experiments had three monopiles spaced 18.5cm on center and in the center of the large box, Fig. 7. They were installed to an approximate depth of 10.16 cm (assuming no or minimal plug heave). Results of only two monopiles from Experiment One will be presented; the third had a rigid connection and initial results are available in Murali, et al. (2015). A mudmat 3D printed in ABS plastic was placed at one end of the box. It carried a 100g MEMS accelerometer (Silicone Design Inc, 2013) at the same level as the 10g accelerometers mounter on the monopiles. Three Linear Variable Differential Transducers (LVDT) were mounted by brackets to the box in order to measure translation of each pile. To monitor pore pressure generated by monopile loading three pore pressure sensors were installed (during model construction) at approximately the mid-depth of the piles (5 cm for Pile 3 and Pile 4 and 5.5 cm Pile 5), 3.81 cm away in the direction of cyclic loading (+X), and the opposite direction of monotonic loading.

Finally, the model was center on the centrifuge basket so all monopiles were in line with the plane of reactive centrifugal acceleration and Earth's gravity.

4 TESTING METHODOLOGY

4.1 Centrifuge Acceleration

Reactive centrifugal acceleration at the centrifuge nominal radius was 70 g. Since the model was beyond the nominal radius recorded acceleration at the height of the sensor platform and the mid-depth of the monopiles was 71.5 g and 73.5 g respectively.

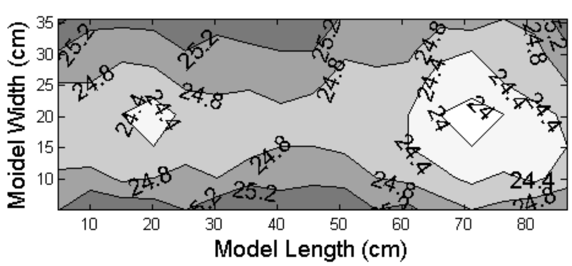

Figure 5. Experiment One post-consolidation topography

Table 1. Water content with depth for Experiment One post-consolidation

Depth (cm)	Water Content (%)
2.24	70.9
4.48	69.9
6.71	68.8
9	68.2
11.2	65.8
13.43	63
15.67	59.8
17.9	57.4
20.14	56.7
22.38	55.3

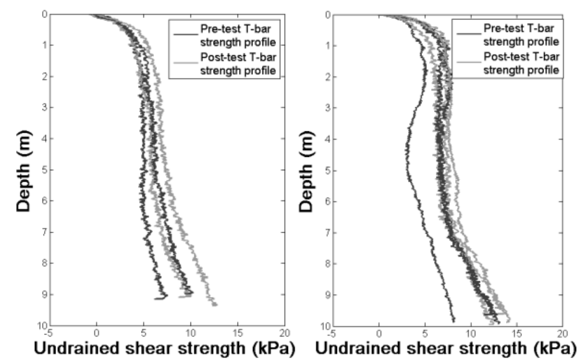

Figure 6. Undrained shear strength for the Experiments One test bed (left) and Experiment Two test bed (right)

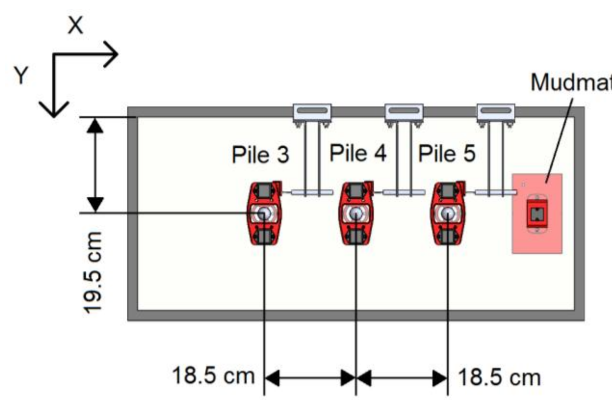

Figure 7. Experiment Two model layout

4.2 Experiments

Two models were spun resulting in two experiments. Results will be presented from two monopiles in Experiment One and all three monopiles in Experiment Two. Experiments consisted of one-way cyclic loading in the +X direction followed by a capacity test in the –X direction. Presented in Table 2 is the capacity test matrix.

Table 2: Capacity test matrix

Monopile	Load Eccentricity	Displacement Magnitude	Load Direction
#	D	D (%)	±X
Experiment One: Virgin			
1	2.5	30	-X
2	1.25	30	-X
Experiment Two: Post-Cyclic			
3	2.5	30	-X
4	1.25	30	-X
5	3.5	30	-X

Where D is monopile diameter. Load eccentricity is taken from the top of the monopile and displacement magnitude is applied at eccentricity. All load direction for the capacity tests were in the -X direction.

Monopiles 3-5 were all cycled under one-way loading; that is, a full cycle was motion in the +X direction followed a return to the initial location. The RPI four DOF robot was used to apply the cyclic load. Given the robots maximum acceleration of 50 mm/s^2, cyclic velocity was set to 2 mm/s to ensure the monopiles were strained at a constant rate over at least 95% of their displacement amplitude. As described in Table 3, each monopile underwent three sets of cycling; of 50 cycles each.

As before load eccentricity is from the monopile cap and displacement is applied at eccentricity. It should be noted that after each half cycle the RPI four DOF robot paused to reoriented itself, this pause though short is inconsistent in duration; so, cycling frequency was slightly nonlinear and random. Each half cycle motion behaved predictably. Additionally, a small vertical downward motion of 0.75 mm was added between cycle 25 and cycle 26 to accommodate pile settlement during cycling. Further results from the cyclic portion of these experiments will be presented at a later date (Beemer, et al., 2016).

4.3 Data Interpretation

For the capacity tests: displacement at the monopile cap was calculated from independent measurements of robot displacement and pile tilt. The RPI 4 DOF robot is capable of measuring its location to the nearest 1 mm. Monopile orientation was determined from measurements of acceleration the 10 g MEMS accelerometer (Beemer, et al., 2015). Essential tilt can be inferred by the proportion of the local reactive centrifugal acceleration measured by the accelerometer.

For the cyclic tests: displacement at the monopile cap was calculated from the LVDT measurement and monopile tilt from the MEMS accelerometer. It was assumed that the pile was infinitely long.

Lateral force and moment was calculated from strain measured in the stem, assuming the stem as a cantilever beam.

Table 3. Cyclic test matrix

Monopile	Load Eccentricity	Displacement Magnitude	Load Direction	Cycles
#	D	D (%)	±X	#
3	2.5	2.5	+X	50
		5	+X	50
		10	+X	50
4	1.25	2.5	+X	50
		5	+X	50
		10	+X	50
5	3.5	2.5	+X	50
		5	+X	50
		10	+X	50

5 RESULTS AND DISCUSSION

5.1 Virgin and Post-Cyclic Results

The load displacement curves for all of the piles tested are presented in Fig. 8 including initial loading (virgin soil) and post-cyclic loading. The lateral head load, H, at the top of the pile cap was computed and normalized by the product of the projected vertical area, LD, and an average shear strength profile over the depth of pile embedment, $S_{u,avg}$. The lateral displacement, y, was computed at the mudline using the tilt and displacement measurements and normalized by the pile diameter, D.

All the piles were pushed laterally at the top of the ball and socket connector to a displacement amplitude equal to 30% of the pile diameter. Thus, the pile displacement amplitude at the mudline varied depending on the eccentricity.

As expected, the ultimate lateral capacity of the piles decreased with increasing eccentricity for both initial and post-cyclic monotonic loading. It was also observed that due to rotational failure mechanism exhibited by short piles, there is an increase in strength as the pile displaces, which also increases the mobilized pressure.

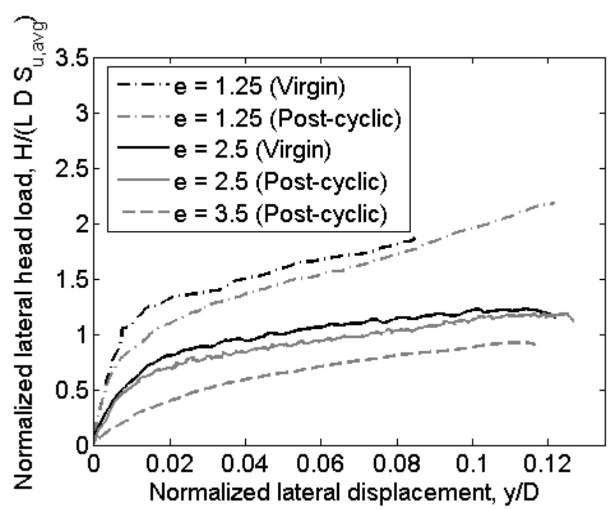

Figure 8: Virgin and post one-way cyclic curve comparison

Fig. 8 shows that, when comparing horizontal bearing factors at the same normalized lateral displacement, the trend (or path) of the post-cyclic capacity is slightly lower than the ultimate capacity. Nevertheless, post-cyclic test presented a higher failure load, at a larger strain when compared to the initial test (virgin soil). The stiffness behavior of the curves show that the variation in slope is greater for the ultimate capacity curves whereas the post-cyclic capacity which varies gradually.

For the piles tested with an eccentricity of 1.25, the stiffness response for both the virgin and post-cyclic curves are elastic and identical to each other until a normalized lateral displacement amplitude of about 0.4% is reached. After this point, the post-cyclic response gradually becomes more plastic. Similarly, for the pile tested with an eccentricity of 2.5, the stiffness response for both the virgin and post-cyclic curves are elastic and identical to each other until a displacement amplitude of 0.65% beyond which the post-cyclic pile response becomes more plastic.

A fair comparison cannot be performed for the pile tested at eccentricity of 3.5 since it was only tested under post-cyclic conditions. A general observation from all the tests is that elastic stiffness appears to decrease with increasing eccentricity for a constant aspect ratio.

5.2 Pore Pressure Generation and Set Up

Post-cyclic monopile capacity can be impacted by the generation and dissipation of pore pressure (or set up) during cycling. Pore pressure generation was monitored during cycling of Pile 4 and 5 (the pore pressure sensor associated with Pile 3 was not operating properly). An overview of pre-cycling, peak, and pre-capacity pore pressures are provided in Table 4.

It can be seen that the smaller eccentricity generated more pore pressure but was not able to dissipate it prior to the post-cyclic capacity test. While the larger eccentricity generated less pore pressures, but were able to dissipate all excess pressure. Resulting in a slight set up of Monopile 5. This can be further seen in the plots of pore pressure over time for cyclic magnitudes of 10% diameter, Fig. 9 and 10.

Table 4. Pore pressure behavior

Monopile	Cyclic Magnitude	Pre-Cycling	Average Peak	Pre-Capacity
#	D (%)	Pore Pressure (kPa)		
4	2.5	32	40	46
	5	41	43	
	10	41	46	
5	2.5	49	51	47.8
	5	48	50	
	10	48	51	

Note: *cyclic magnitude is at eccentricity.*

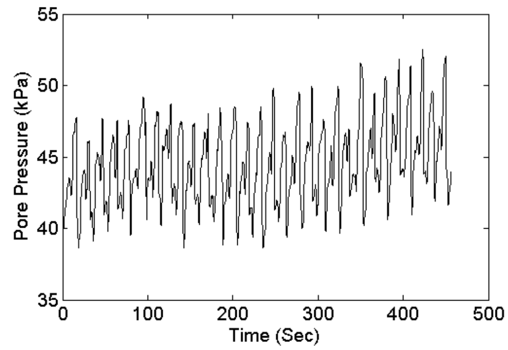

Figure 9: Monopile 4 pore pressure during 10% displacement

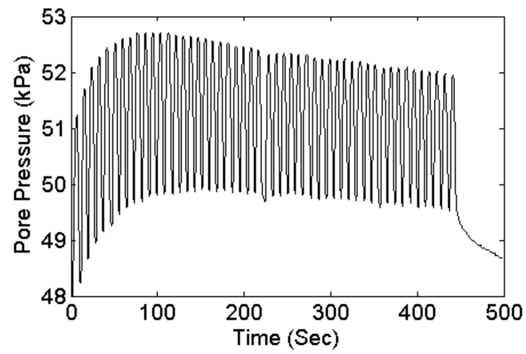

Figure 10: Monopile 5 pore pressure during 10% displacement

These figures clearly show pore pressure readily dissipates had higher eccentricity, but not lower. This may be due to the cyclic displacement magnitude. Though displacement at eccentricity is the same for both monopiles (10%) displacement at the soil surface was not; for Monopile 4 it was 4% diameter and for Monopile 5 it was 2% diameter. It is possible that more remoulding, at higher displacement magnitudes, increases the coefficient of consolidation and reduces the rate of pore pressure dissipation. More tests at lower eccentricities with additional cycles (>50) will be need to investigate this.

5.3 Comparison to simplified upper bound formulation

Fig. 11 presents analytical bearing capacity curves computed for a monopile of *L/D* of 2, with eccentricities ranging from 0 to 4. A uniform undrained shear strength profile was assumed. A number of cases were considered for the upper bound analysis, curves are presented for an adhesion factor, α, of 0 (smooth case), 0.5 and 1 (rough case). The bearing factors curves were also computed assuming gapping (no suction) and no gapping (suction) at the back of the monopile. The centrifuge experimental data points for both virgin and post-cyclic tests are also presented on Fig. 11. The failure points were selected at a strain of 5 % to compare with plasticity model which is a small strain analysis.

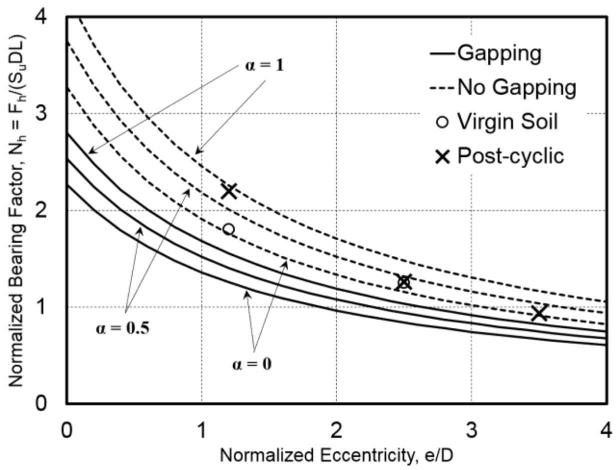

Figure 11: Comparison of experimental data with simplified upper bound solution

It can be seen from the plot that the centrifuge experimental data follows the trend of the analytical curves and compares fairly well, specifically for the cases of suction developing at the back of the monopile. Although the presence of slight gapping was noticed for certain pile tests at the end of all the centrifuge tests, the gapping depths extended to varying depths along the length of the pile and could not be accurately quantified for the different model pile tests.

Another area of possible source of error was the plastic coating applied on the piles to prevent corrosion of the strain gages. It was not possible to quantify the adhesion on the sides of the pile.

6 CONCLUSIONS

This paper reports a series of centrifuge pile tests that were carried out to examine the behavior of short aspect ratio piles, specifically *L/D* = 2. The virgin and post-cyclic response of the monopile foundation was examined and compared with a simplified upper bound plasticity analysis. The following are the key points summarized from the results:

- On comparing virgin and post-cyclic capacity, it was found that the capacities were similar with the post-cyclic response slightly lesser at the same displacement amplitudes.
- The change in stiffness is more gradual for the post-cyclic tests as compared to the undisturbed test results. It was also found that linear elastic stiffness decreased with increasing eccentricity.
- The experimental bearing factors compared significantly well with the plasticity analysis after Aubeny et. al. (2003) for the case of no gapping at the back of the monopile.
- Though higher pore pressures are generated at lower displacement magnitudes, they dissipate more readily at higher displacement magnitudes.
- Pore pressure behavior indicate practically no set up of Monopile 4 prior to capacity testing. Pore pressures indicates set up of Monopile 5 due to cycling, but the magnitude of set up is likely low given the values of pore pressures generated.

ACKNOWLEDGEMENT

The authors acknowledge the assistance provided by the personnel at Rensselaer Polytechnic Institute and the Dept. of Aerospace Engineering at Texas A&M University. We also acknowledge the help provided by our colleagues at the Zachry Dep. Of Civil Engineering. This project is funded by the National Science Foundation, Award Number: 1041604.

REFERENCES

Andersen, K., Murff, J., Randolph, M., Cluckey, E., Erbrich, H., Jostad, H., Hansen, B., Aubeny, C., Sharma, P. and Supachawarote, C. 2005. Suction anchors for deepwater applications*. In Frontiers in Offshore Geotechnics: ISFOG 2005.* Taylor and Francis.

Aubeny, C., Murff, J.D. and Moon, S.K. 2001. Lateral undrained resistance of suction caisson anchors. *Int. J. of Offshore Polar*. 11(2):95-103

Aubeny, C., Han, S.W. and Murff, J.D. 2003. Inclined load capacity of suction caissons. *Int. J. for Numer. and Anal. Met.* 27(14):1235-1254

Aubeny, C. and Murff, J.D. 2005. Simplified limit solutions for the capacity of suction anchors under undrained conditions. Ocean Engineering. 32:864-877

Beemer, R. D., Murali, M., Biscontin G. and Aubeny, C. 2015. Theory on measuring orientation with mems accelerometers in a centrifuge. *International Foundations Congress and Equipment Expo* (IFCEE), San Antonio.

Beemer, R. D., Murali, M., Aubeny, C and Biscontin G. 2016. Rotational stiffness of squat monopiles in soft clay from centrifuge experiments. Manuscript in preparation.

Cluckey, E., Aubeny, C. and Murff, J.D. 2004. Comparison of analytical and centrifuge model tests for suction caissons subjected to combined load. *J. Offshore Mech. Arct.*, 126, 364-367

Dejong, J., Yafrate, N., Degroot, D., Low, H. E., and Randolph, M. 2012. Recommended practice for full-flow penetrometer testing and analysis. *Geotech. Test. J.*, 33(2).

Elgamal, A., Dobry, R., and Van Laak, P. 1991. Design, construction and operation of 100 g-ton centrifuge at RPI. *Centrifuge 91*, Boulder, CO, 27–34.

Hamilton, J., Phillips, R. Dunnavant, T. and Murff, J. 1991. Centrifuge study of laterally loaded piles in soft clay. *Proc. of Int. Conference Centrifuge*, ISSMFE.

Jeanjean, P. 2009. Re-Assessment of P-Y Curves for Soft Clays from Centrifuge Testing and Finite Element Modeling. O*ffshore Technology Conference*, Houston, 1–23.

Ladd, C. C., and Foott, R. 1974. New Design Procedure for Stability of Soft Clays. *J. of Geotech. Eng*., ASCE, 100(7), 763–786.

MEMSIC Inc. n.d.. CXL-GP series general purpose accelerometer. San Jose, CA.
Murali, M., Grajales, F., Beemer, R. D., Biscontin, G. and Aubeny, C. 2015. Centrifuge and numerical modeling of monopiles for offshore wind towers in clay. *34rd International Conference on Ocean, Offshore and Arctic Engineering* (OMAE2015-41332), St. John's, Newfoundland, Canada.
Murff, J.D. and Hamilton, J.M. 1993. P-Ultimate for undrained analysis of laterally loaded piles. *J. of Geotech. Eng.*, ASCE, 119(1): 91-107.
Murff, J.D. 1996. "The geotechnical centrifuge in offshore engineering" (OTC8265), *Offshore Technology Conference*, Houston, Texas, USA.
Pokrovsky, G. I., and Fyodorov, I. S. 1936. Studies of soil pressures and deformations by means of a centrifuge. *1st International Conference on Soil Mechanics and Foundation Engineering*, Harvard, Cambridge, MA, 70.
Randall, R. 2010. *Elements of ocean engineering*. 2nd edition. Society of Naval Architects and Marine Engineers (SNAME).
Randolph, M.F. and Houlsby, G.T. 1984. "The limiting pressure on a circular pile loaded laterally in cohesive soil." *Geotechnique.* 34(4):613-623.
Schneider, J. and Senders, M. 2010. Foundation design: a comparison of oil and gas platforms with offshore wind turbines. *Mar. Technol. Soc. J.* 44(1):32-51
Shapeways. n.d.. "Stainless steel specifications." Material Data Sheet, New York City.
Silicon Design Inc. 2013. Model 2012. Kirkland, WA.
Tessari, A., 2012. Centrifuge modeling of the effects of natural hazards on pile-founded concrete floodwalls. PhD Dissertation, Rensselaer Polytechnic Institute.
Ubilla, J., Abdoun, T., and Zimmie, T. 2006. Application of in-flight robot in centrifuge modeling of laterally loaded stiff pile foundations. *6th ICPMG '06*, Taylor & Francis, Hong Kong, 259–264.
Zhang, C., White, D. and Randolph, M. 2011. Centrifuge modeling of the cyclic lateral response of a rigid pile in soft clay. *J. of Geotech. Geoenviron.* 137(7) 717-729.

APPENDIX I - MATHEMATICAL EXPRESSIONS FOR SIMPLIFIED PLASTIC LIMIT ANALYSIS METHOD.

The following is a brief summary of the main mathematical expressions needed to understand Aubeny et al. (2001) simplified upper bound method.

It is assumed that the monopile is subject to a virtual velocity field as the one presented in Fig. A1. Which is produced by the application of a virtual angular velocity β about a center of rotation *O*.

Assuming a constant soil shear strength profile, an estimate of the collapse load (*F*) can be found by equating the rate of internal energy dissipation to the external work, as described in equation A1.

$$F = \left(\dot{D}_s + \dot{D}_e\right)\left|1 - \frac{L_i}{L_0}\right|^{-1} \quad \text{[A1]}$$

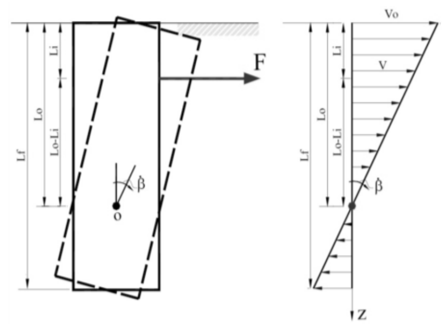

Figure A.1: Equivalent virtual velocity field for a laterally loaded monopile. (From: Aubeny et al, 2001)

In equation a1, the dissipation rate due to side resistance ($\dot{D}_s$) is given by:

$$\dot{D}_s = v_0 D \int_0^L \left|1 - \frac{z}{L_0}\right| \left(N_p s_u + \gamma' z\right) dz \quad \text{[A2]}$$

Where: *D* is the monopile diameter, *L* is the monopile length, L_0 is the depth to the center of rotation, v_0 is the velocity at the top of the monopile, z is the depth, s_u is the undrained shear strength and γ' is the buoyant weight of soil. Finally, N_p is given as described in equation 1 on this paper.

The internal energy dissipation due to end resistance $\dot{D}_e$ is given by Murff and Hamilton (1993) by the following expression:

$$\dot{D}_e = \frac{v_0 R_2^3}{L_0} \int_{\phi=0}^{\phi=2\pi} \int_{\omega=0}^{\omega=\sin^{-1}(R/R_2)} s_u \sin\omega \sqrt{\cos^2\omega + \sin^2\omega \sin^2\phi}\, d\omega d\phi \quad \text{[A3]}$$

Where: R is the monopile radius, R_2 is the radius of the spherical failure surface, ϕ is the angular coordinate about the monopile centerline in a horizontal plane (0 to 2π) and ω is the angular coordinate from the monopile centerline. (See Fig. A2).

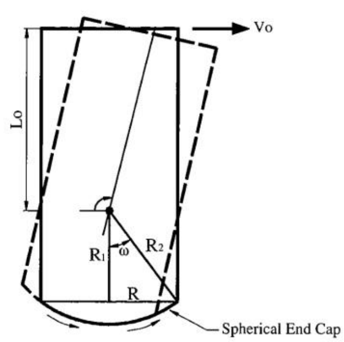

Figure A.2: Spherical end failure mechanism (From: Aubeny et al, 2003)